J Solid State Electrochem (2009) 13:935–942
DOI 10.1007/s10008-008-0636-x

ORIGINAL PAPER

Relationships between microstructure and pitting corrosion of ADI in sodium chloride solution

H. Krawiec · J. Lelito · E. Tyrała · J. Banaś

Received: 16 May 2008 / Revised: 11 July 2008 / Accepted: 21 July 2008 / Published online: 8 August 2008

Abstract Austempered ductile iron (ADI) has complex microstructure containing a multiphase matrix (called 'ausferrite'), graphite spheres and oxide inclusions. The corrosion resistance of ADI is related to its microstructure which is determined by heat treatment parameters (like austempering temperature, austempering time, austenitising temperature and austenitising time). In the present paper, the electrochemical behaviour and corrosion resistance of ADI have been investigated by means of the electrochemical microcell technique and classical electrochemical measurements in sodium chloride solution. Particular attention has been paid to the influence of austempering temperature on the microstructure and pitting corrosion. It has been shown that ADI austempered at 430 °C has upper ausferritic microstructure and reveals a better corrosion resistance in sodium chloride solution than ADI austempered at 280 °C. Moreover, the corrosion resistance increases as the volume fracture of ferrite increases and the carbon content of austenite decreases. The good corrosion behaviour of ADI austempered at 430 °C was also related to the good coarsening of the austenite grains and broad ferrite needles (less ferrite/austenite interfaces). It has been demonstrated that silicon is the alloying element hindering the anodic dissolution of the alloy.

Keywords Austempered ductile iron · Local electrochemistry · SIMS · Anodic dissolution

H. Krawiec (✉) · J. Lelito · E. Tyrała · J. Banaś
Faculty of Foundry Engineering,
AGH-University of Science and Technology,
Reymonta 23 Street,
30-059 Cracow, Poland
e-mail: krawiec@agh.edu.pl

Introduction

Austempered ductile iron (ADI) has many attractive properties such as an unusual combination of high strength and ductility, good wear resistance and high fatigue strength [1–6]. These excellent mechanical properties are related to the particular microstructure of ADI called "ausferrite" that consists of ferrite (α) and high carbon austenite (γ_{HC}). It is well known that the morphology of ferrite and austenite, their volume fraction and the carbon content of the austenite depend on the heat treatment conditions. The influence of the heat treatment parameters (austenitising time, austenitising temperature, austempering time and austempering temperature) on the evolution of the microstructure and the mechanical properties have been studied [4, 7–10]. ADIs austempered at low temperatures have high hardness, high strength and low ductility. It has been found that strength decreases with increasing austempering temperature, whilst the ductility increases simultaneously. High austempering temperatures (over 350 °C) give typically upper ausferritic microstructure, which consists of broad blades of isolated ferrite. This microstructure results with a high tensile toughness. Similar microstructures have been observed at high austenitising temperatures. The length of the ferrite needles was generally found to increase with increasing austenitising temperature. This phenomenon has been attributed to the greater coarsening of austenite grains at the high austenitising temperatures [4]. The length of the largest ferrite needles can be assumed to represent the prior austenite grain size.

The corrosion behaviour like mechanical properties is related to the alloy microstructure. A survey of the literature indicates that some attention has been paid to the corrosion resistance of ADI. Hemanth [11] has found, using the weight loss method defined in the ASTM G67-80 stand-

ards, that the corrosion resistance of ADI depends on the microstructure of cast iron. Austempering temperature and time have an influence on the quantity of microstructure constituents of ausferrite. The matrix of only ausferrite is better than that of perlitic structure obtained without chilling and austempering. Moreover, the Ni and Mo content combination of austempered chilled ductile iron, together with chilling and austempering, both contribute to its superior corrosion resistance. However, Pepe et al. [12] have improved the corrosion resistance of ADI by sol–gel organic–inorganic hybrid coatings. ADI exhibits a completely different electrochemical behaviour in hot concentrated sulphuric acid compared to the aqueous solution containing Cl^- or ClO_4^- ions. Anodic dissolution of ADI in concentrated H_2SO_4 is divided into three stages proceeding with oxidation of iron (only this stage occurs in chloride-based media), formation of iron sulphate and oxyhydroxide [13]. Moreover, the corrosion products have formed on ADI a porous surface layer where silicon oxide SiO_2 is the major component in 96% H_2SO_4 solution. The corrosion behaviour of ADI in alkaline sodium perchloride solution has been investigated by means local electrochemical techniques [14]. Surface observations combined with local electrochemical analysis have shown that corrosion of ADI first occurs in the close vicinity of some graphite spheres and then around oxide inclusions. The oxidised regions are richer in oxygen than the matrix located far from spheres.

In this paper, the relationships between the microstructure and pitting corrosion of ADI have been investigated in 1 M NaCl by means of electrochemical measurements (potentiodynamic polarization curves and chronoamperometry) conducted at the macro- and microscale. Changes in the morphology and chemical composition of the surface were determined after corrosion tests using secondary ion mass spectroscopy (SIMS) and field emission (FE)-SEM/energy-dispersive spectroscopy (EDS). The corrosion behaviour of alloys was then related with their microstructure (lower or upper ausferritic microstructure). Besides the good mechanical properties, high corrosion resistance properties will ensure a wider application field for ADI.

Experimental

In order to obtain ADI, ductile iron (DI) with perlitic microstructure was used as initial material. The chemical composition of ductile iron used in this experiment was C, 3.48 wt.%; Mn, 0.63%; Si, 2.58%; P, 0.03%; S, 0.017%; Cr, 0.06%; Ni, 0.04%; Cu, 0.32%; Mg, 0.054%; Mo, 0.07%; Ti, 0.015%; Sn, 0.006%; Pb, 0.001%; V, 0.009%; W, 0.038%; Zn, 0.003. Ductile iron was poured into Y block moulds. The Y block was cut into cylindrical specimens with diameter × length equal to 10×70 mm. Two austempered holding temperatures (280 °C and 430 °C) were selected. The heat treating procedures were as follows: (1) austenitising at 900 °C for 2 h, (2) austempering at 280 °C and 430 °C for 2 h, (3) water cooling to room temperature of 25 °C. The heat treatment was performed in a salt bath furnace. Before electrochemical treatment, ADI specimens were mechanically ground with silicon carbide (SiC) emery papers down to 4,000 grit and polished with diamond pastes down to 1 μm. They were ultrasonically rinsed in ethanol between each step.

Global electrochemical measurements were carried out on disks (which were insulated by coating with a cataphoretic paint and embedded in an epoxy resin) using a classical three-electrode cell. A Voltalab PGZ301 electrochemical interface was used in the experiments. The counter electrode was a platinum disk of 10-mm radius and the saturated calomel electrode was used as a reference electrode. A cathodic potential of −800 mV vs. saturated calomel electrode (SCE) was first applied for 3 min, after which the potentiodynamic polarisation curves were determined in 1 M NaCl at a scan rate of 1 mV s^{-1}. The chronoamperometry measurements were performed at chosen potential values.

The local electrochemical behaviour of the matrix, inclusions and carbon spheres was studied from potentiodynamic measurements carried out at 25 °C using the electrochemical microcell technique [15] with 20- to 50-μm microcapillaries. As the specimen surface which is in contact with the electrolyte was very small (of about 1,500 μm^2) and the current measured was extremely low (in the range of pA within the passive range), the electrochemical setup was placed in a Faraday cage and a modified high-resolution potentiostat was used in order to have a current detection limit of 20 fA (Jaissle 1002T-NC-3). All the potentials were measured versus a SCE and a platinum wire counter electrode. A cathodic potential of −800 mV vs. SCE was first applied for 3 min, after which the potentiodynamic polarisation curves were determined in 1 M NaCl, at a scan rate of 1 mV s^{-1}.

SIMS analyses were performed using a MIQ 256 Cameca Riber apparatus located in a ultra-high vacuum chamber (of about 10^{-7} Pa). Repartition of $^{28}Si^+$, $^{56}Fe^+$, $^{12}C^-$, $^{35}Cl^-$ and $^{16}O^-$ ions on sites containing carbon spheres was obtained using Ar^+ primary ion source (10 keV, incident angle of 45°). Acquisition of the images (128×128 pixels) was performed without preliminary sputtering and by applying a current of 5 nA and a dwell time of 3.66×10^{-3} s/pixel. These parameters were chosen to minimise the consumption of matter during analysis.

A field-emission-type scanning electron microscope (JEOL 6400F) with an integrated electron dispersion spectrometer (FE-SEM/EDS) was used in order to determine the morphology and the chemical composition of spheres, inclusions and the surrounding matrix at the microscale. On

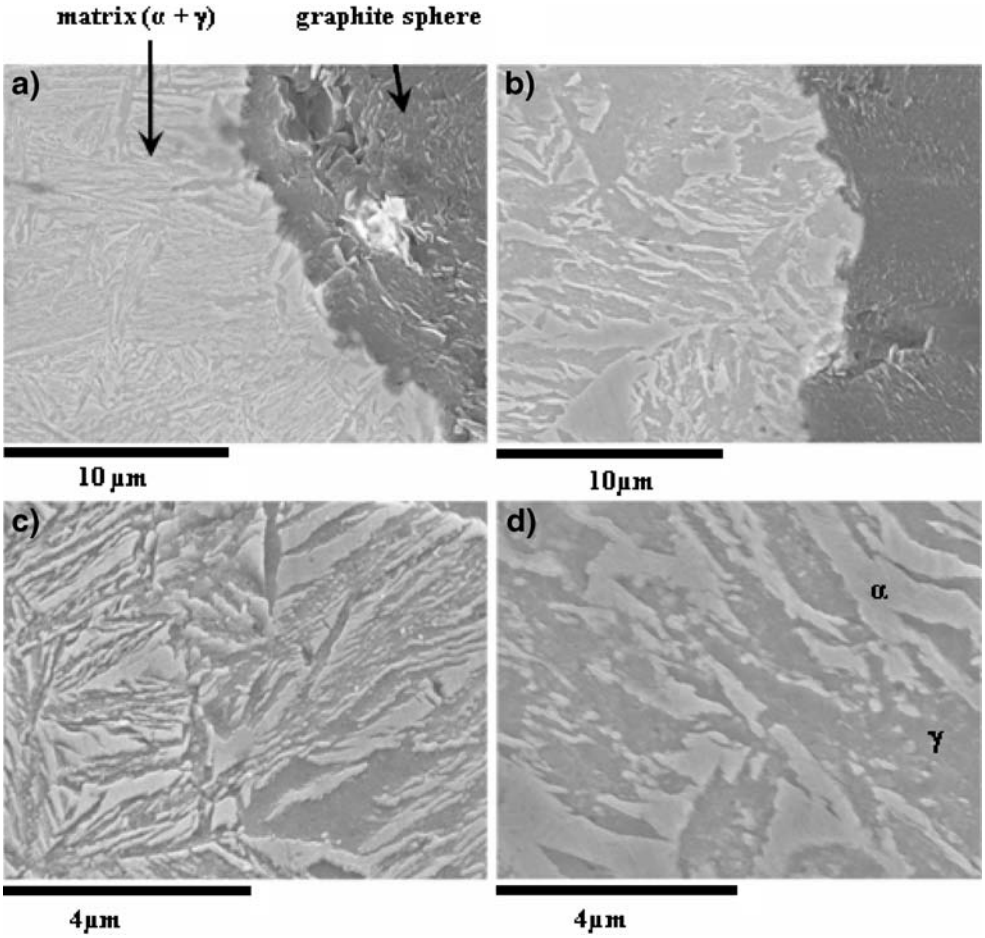

Fig. 1 SEM micrographs of the ADI microstructure revealed after etching in 4% HCl–C_2H_5OH solution for 2 min at 25 °C and two different austempering temperatures: **a**, **c** for ADI T_{It}=280 °C and **b**, **d** for ADI T_{It}=430 °C

the other hand, X-ray diffraction (XRD) analysis was conducted for phase identification using diffractometer Philips (type PW1710 Based) and Co-Kα (wavelength, λ=1.788 Å) radiation. Quantitative estimation of the volume fraction was performed by using the APD 3.5B software.

Results and discussion

Microstructure and chemical analysis of ADI after polishing

The special heat treatment of ductile iron described in the experimental section yields the ADI microstructure consisting of ferrite (α) needles in a stabilised high carbon austenite (γ_{HC}) matrix (auferrite microstructure). This microstructure has been revealed after etching in Nital (4 wt.% HCl–C_2H_5OH) solution, as shown in Fig. 1, for austempering temperatures of 280 °C and 430 °C. The observations performed by FE-SEM revealed that the samples austempered at 280 °C (noted ADI, 280 °C) have a lower ausferritic microstructure consisting of very fine needles of ferrite, as shown in Fig. 1a,c. By contrast, the samples austempered at 430 °C (noted ADI, 430 °C) have typical broad ferrite needles of the upper ausferritic microstructure (Fig. 1b,d). ADI (280 °C) contains about 18.2 vol.% austenite and 81.8 vol.% ferrite, whereas ADI (430 °C) contains about 12.1 vol.% austenite and 87.9 vol.

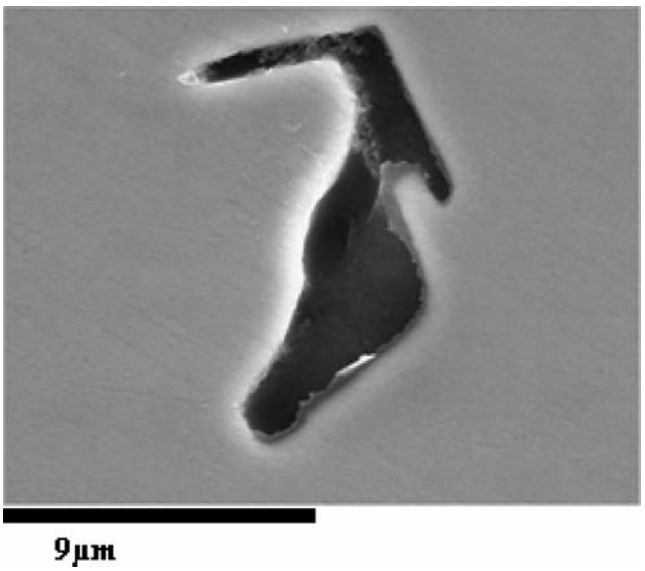

Fig. 2 SEM micrograph of an oxide inclusion present in the matrix revealed after polishing of ADI austempered at 430 °C

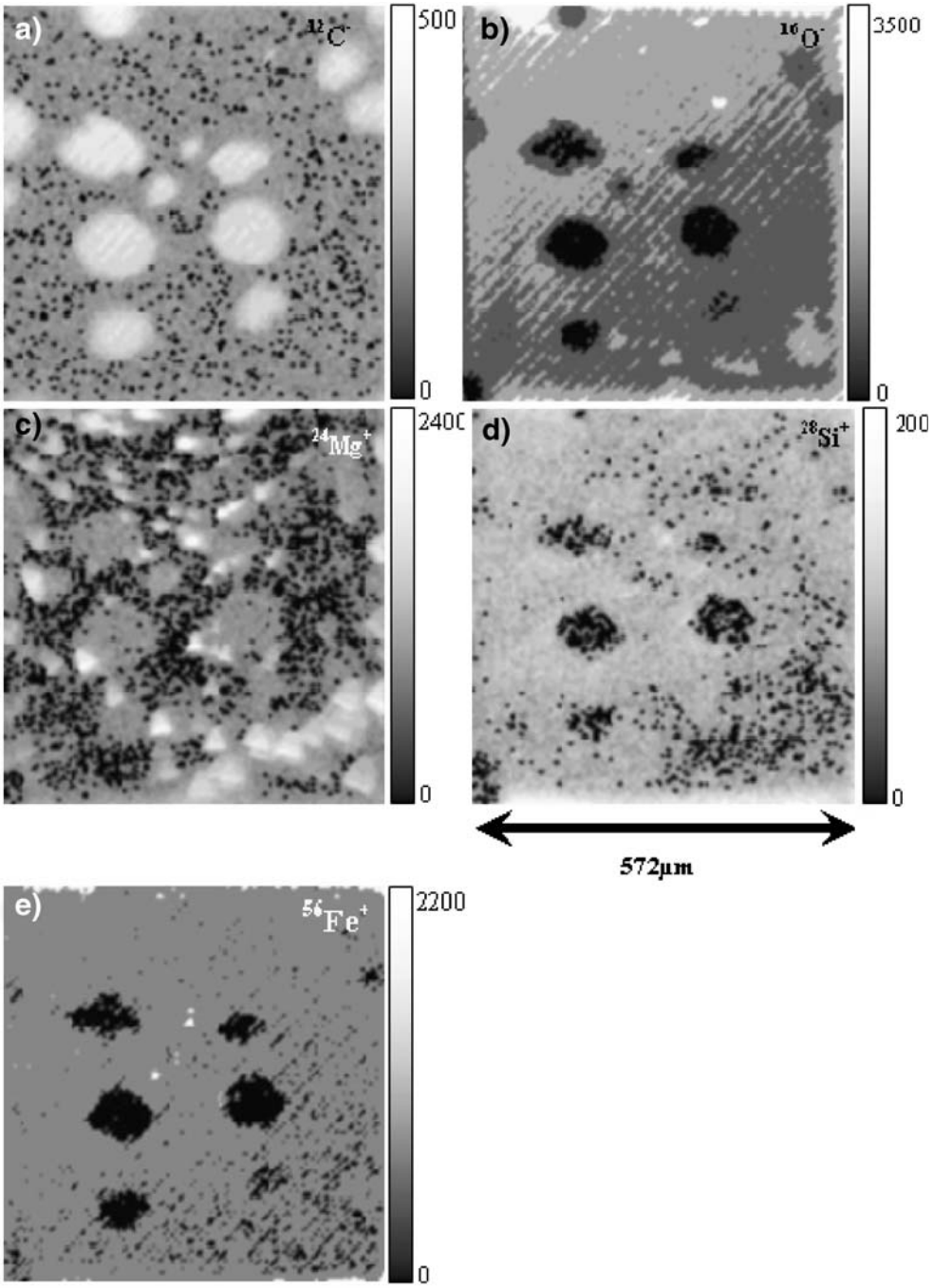

Fig. 3 Repartition of ionic species: **a** carbon $^{12}C^-$, **b** oxygen $^{16}O^-$, **c** magnesium $^{24}Mg^+$, **d** silicon $^{28}Si^+$, **e** iron $^{56}Fe^+$ determined from SIMS experiments on sites containing the matrix and some graphite spheres (under Ar^+ primary ions) after mechanical polishing for ADI austempered at 430 °C

% ferrite. These values were obtained from XRD measurements. It has been found [4, 16] that the austenite content increases with increasing austempering temperature in the range of 250–400 °C. However, at very high temperatures (above 400 °C), the diffusion rate of carbon is too rapid to meet the demand of phase transformation. Consequently, the volume fracture of austenite starts to decrease [4, 16], as it was observed at 430 °C. The second important microstructure parameter estimated by XRD is the carbon content of austenite (Cγ) which was determined using the following equation [17]:

$$a_\gamma = 0.3548 + 0.0044C_\gamma \quad (1)$$

where a_γ is the lattice parameter of austenite in nanometer (obtained from XRD measurements) and Cγ is the carbon content of austenite in weight percent. The carbon content of the austenite was 2 and 1.45 wt.% for samples austempered at 280 °C and 430 °C, respectively.

Detailed analysis by means of FE-SEM/EDS exhibited the presence of small and elongated oxide inclusions (size between 3 and 12 μm) in both sets of specimens, as shown in Fig. 2. The average chemical composition of these inclusions was: O, 50.0 at.%; Mg, 22 at.%; Si, 0.1 at.%; Fe, 12 at.%. The oxide inclusions were mixture of magnesium and iron oxides (MgO and FeO) with a small amount of silicon dioxide SiO_2. SIMS measurements performed on ADI after mechanical polishing indicated that carbon is located in the spheres (Fig. 3a). Local enrichment of magnesium was detected at the inclusion surface, Fig. 3c. The distribution of silicon (Fig. 3d), oxygen (Fig. 3b) and iron (Fig. 3e) in the matrix was rather homogenous. Similar distribution of the elements was observed after mechanical polishing on ADI (280 °C). The results presented above show that the austempered temperature has influence on the ausferritic microstructure, especially on the size of ferrite needles. Considering these properties of ADI samples, their electrochemical behaviour has been investigated in 1 M NaCl solution.

Influence of the microstructure on electrochemical behaviour of ADI at the macroscale

The global polarisation curves were determined on ADI samples obtained at the two austempering temperatures (280 °C and 430 °C, black and grey curves, respectively), as shown in Fig. 4a. This was done to identify the corrosion mechanisms depending on the austempering temperature and the microstructure. The corrosion potential for ADI (280 °C) and ADI (430 °C) was −675 mV/SCE and −540 mV/SCE, respectively, as shown in Fig. 4, indicating that austempering at higher temperature (upper ausferritic microstructure) shifts the corrosion potential to the anodic direction. This suggests that ADI (280 °C) is more active than ADI (430 °C). For both samples, the current density sharply increases above the corrosion potential to reach a limiting value of about 50 mA/cm^2 at −300 mV/SCE. Such a corrosion behaviour results from an anodic process, corresponding to iron dissolution (Eq. 2) and a cathodic process (Eq. 3). In aerated sodium chloride solution, the reduction of dissolved oxygen is considered (Eq. 3).

$$Fe = Fe^{2+} + 2e^- \quad (2)$$

$$O_2 + 2H_2O + 4e^- = 4OH^- \quad (3)$$

The hydroxyl ions (OH^-) react with Fe^{2+} ions to form iron hydroxides according to the reactions:

$$Fe^{2+} + 2OH^- = Fe(OH)_2 \quad (4)$$

$$Fe(OH)_2 + OH^- = Fe(OH)_3 + e^- \quad (5)$$

Dehydratation of $Fe(OH)_3$ leads to the formation of Fe_2O_3 according to the reaction:

$$2Fe(OH)_3 = Fe_2O_3 + 3H_2O \quad (6)$$

Iron oxide is the main component of corrosion products. Besides the electrochemical dissolution of iron, electrochemical dissolution of graphite has to be taken into consideration. According to the potential–pH equilibrium diagram for the system carbon–water [18], at 25 °C, graphite exhibits a narrow stability domain. Graphite undergoes oxidation with the formation of carbon dioxide CO_2, carbonic acid H_2CO_3, carbonates HCO_3^- and/or CO_3^{2-},

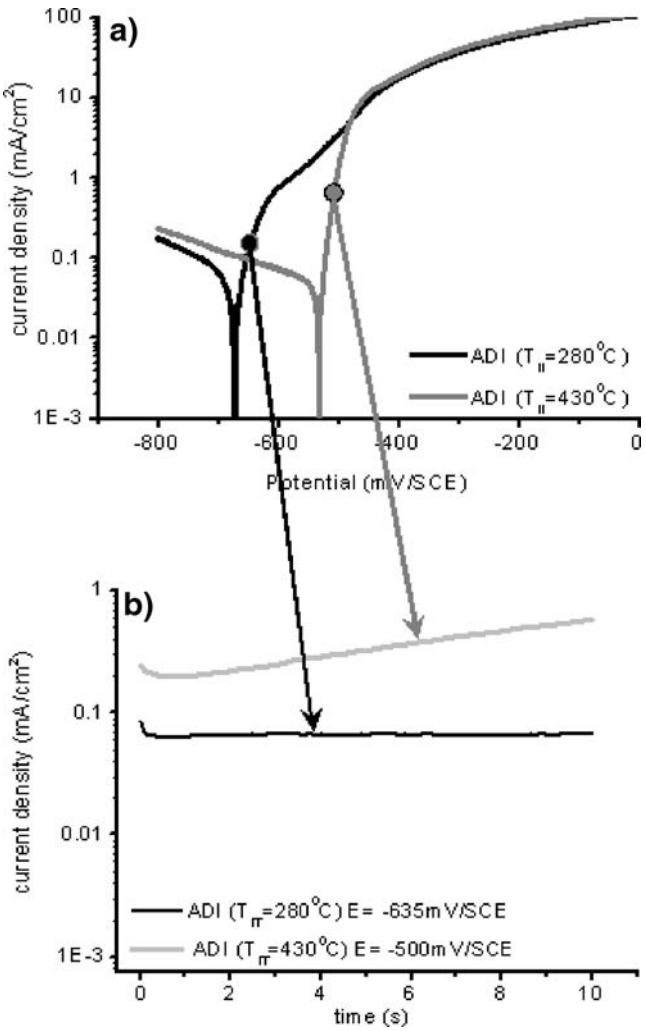

Fig. 4 **a** Global polarisation curves at 1 mV s^{-1} determined on ADI at different austempered temperatures (T_{It}=280 °C, *black curve* and T_{It}= 430 °C, *grey curve*). **b** Chronoaperometry curves at various potentials for 10 s determined on ADI specimens in 1 M NaCl solution

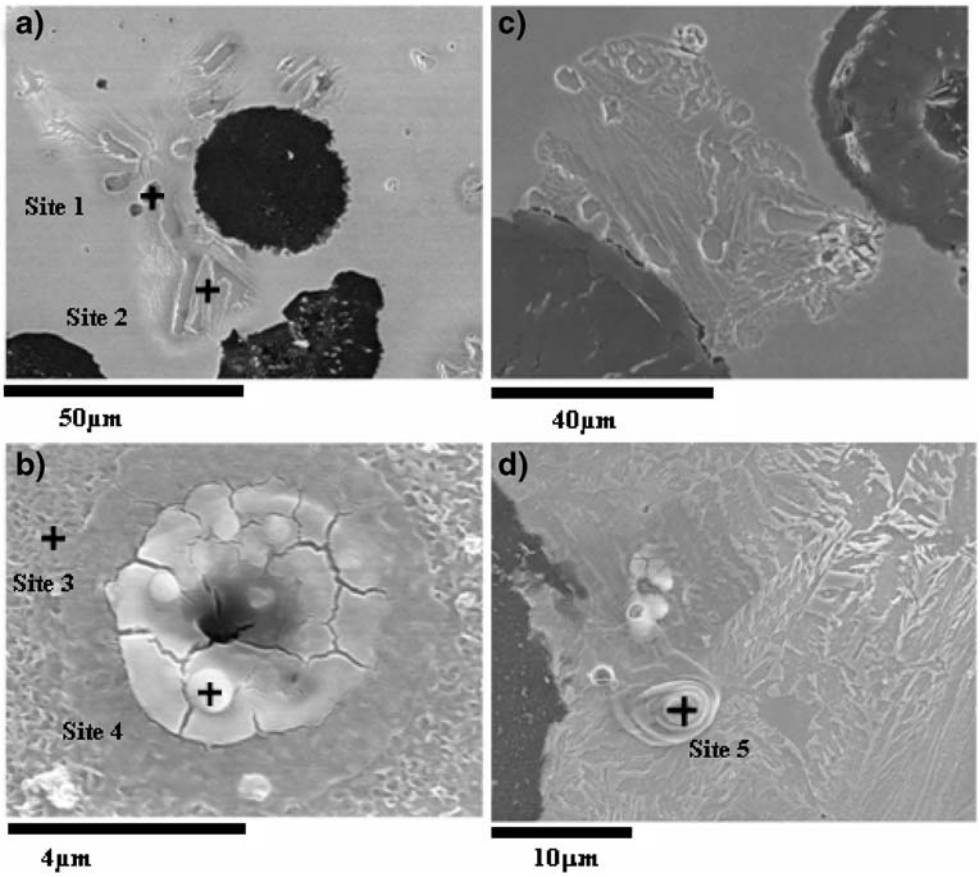

Fig. 5 **a**, **b** SEM micrographs of ADI austempered at 280 °C after global corrosion test in 1 M NaCl solution at −635 mV/SCE for 10 s. **c**, **d** SEM micrographs of ADI austempered at 430 °C after global corrosion test in 1 M NaCl solution at −500 mV/SCE for 10 s

depending on the value of potential and pH. The following electrochemical reactions were proposed:

$$C + 3H_2O = HCO_3^- + 5H^+ + 4e^- \quad (7)$$

$$C + 3H_2O = CO_3^{2-} + 6H^+ + 4e^- \quad (8)$$

$$C + 2H_2O = CO_2 + 4H^+ + 4e^- \quad (9)$$

$$C + 3H_2O = H_2CO_3 + 4H^+ + 4e^- \quad (10)$$

In aqueous solution pH=6, dissolution of graphite starts at about −100 mV/SHE according to reaction 10. This leads to the acidification of the solution.

In order to identify precursor sites for pitting corrosion, global chronoamperometry was performed for 10 s at an overpotential value of 40 mV vs. SCE, corresponding to an applied potential of −635 mV/SCE black line in Fig. 4b for ADI 280 °C and −500 mV/SCE grey curve in Fig. 4b for ADI 430 °C. The course of the chronoaperometric curves revealed that the current increases with the time for ADI 430 °C. The total charge consumed on the whole surface was 2.7 mC 3.4 mC/cm^2 instead of 0.5 mC 0.64 mC/cm^2 on ADI 280 °C. Surface observations performed after these tests revealed that corrosion of both ADI samples starts at some graphite/matrix interfaces and around oxide inclusions Fig. 5a,c. In both cases, the oxidised regions sites 1, 2 in Fig. 5a and site 3 in Fig. 5b contain between 10 and 28 at.% of oxygen and between 50 and 67 at.% of iron, as reported in Table 1. The regions with the corrosion products site 4 in Fig. 5b and site 5 in Fig. 5d are enriched in oxygen 34–57.7 at.% and depleted in iron 26.3–41 at.% and silicon

Table 1 Chemical composition of sites reported in Fig. 5 determined from FE-SEM/EDS experiments

Sites	C at.%	O at.%	Si at.%	Fe at.%
Oxidised regions				
Site 1 in Fig. 6a	20.8	27.6	2.3	49.3
Site 2 in Fig. 6a	19.3	10.7	3.5	66.6
Site 3 in Fig. 6b	21.2	12.3	2.4	64.0
Corrosion products				
Site 4 in Fig. 6b	22.0	34.2	2.8	41.0
Site 5 in Fig. 6d	14.6	57.7	1.5	26.3
Alloy bulk	14.0	–	4.5	81.5

1.5–2.8 at.% with respect to the alloy bulk, as reported in Table 1.

Global electrochemical measurements suggest that the samples with the upper ausferritic microstructure austempered at 430 °C are less prone to pitting corrosion and that oxide inclusions and some graphite/matrix interfaces constitute precursor sites on both samples austempered at 430 °C and 280 °C. The changes observed in the corrosion resistance was related to the microstructural modifications induced by austempering at 430 °C which results to greater coarsening of the austenite grains and broad ferrite needles. It is well known that grain boundaries are defects that could be more sensitive to corrosion. Hence, greater coarsening produces less ferrite/austenite interfaces, leading to the better electrochemical behaviour of ADI in sodium chloride solution.

Influence of the microstructure on electrochemical behaviour of ADI at the microscale

In order to confirm that the corrosion resistance of ADI 430 °C is higher than ADI 280 °C, local polarisation curves were performed using 20- to 50-μm microcapillaries, as shown in Fig. 6. Local polarisation curves obtained on sites of ADI 430 °C containing the pure matrix located far from graphite spheres exhibit systematically a large passive range with current densities of about 1 μA/cm^2, from the potential corrosion up to 800 mV/SCE, as shown in Fig. 6a. Note that no stable pits were detected within the potential range investigated. By contrast, current densities in the range of 3–11 μA/cm^2 were measured on the matrix of ADI 280 °C located far from graphite spheres and stable pitting was often observed at roughly 600 mV/SCE. On both samples, the matrix close to graphite spheres was found to be more sensitive to pitting corrosion than the matrix far from spheres Fig. 6b. Stable pitting was systematically observed at −140 mV/SCE on ADI 280 °C, whereas stable pits were occasionally found on ADI 430 °C above 0 mV/SCE. Sites of both specimens containing the matrix with a single oxide inclusion exhibit stable pitting in the range of 100–400 mV/SCE, as shown in Fig. 6c. Nevertheless, stable pits initiated at lower potentials on ADI 280 °C than ADI 430 °C.

Therefore, local measurements have clearly shown that ADI 430 °C has higher corrosion resistance than ADI 280 °C. The higher corrosion resistance of ADI 430 °C can be related to the lower carbon content of austenite 1.45 wt.%. Additionally, the high volume fracture of ferrite in the material 88 vol.% for ADI, 430 °C ensures a high content of silicon in this phase and hence a better corrosion resistance. Silicon has high affinity to oxygen and easily forms SiO_2 oxide layer, which hinders the corrosion process. It has been shown that corrosion processes start at graphite/matrix interfaces. Furthermore, these interfaces

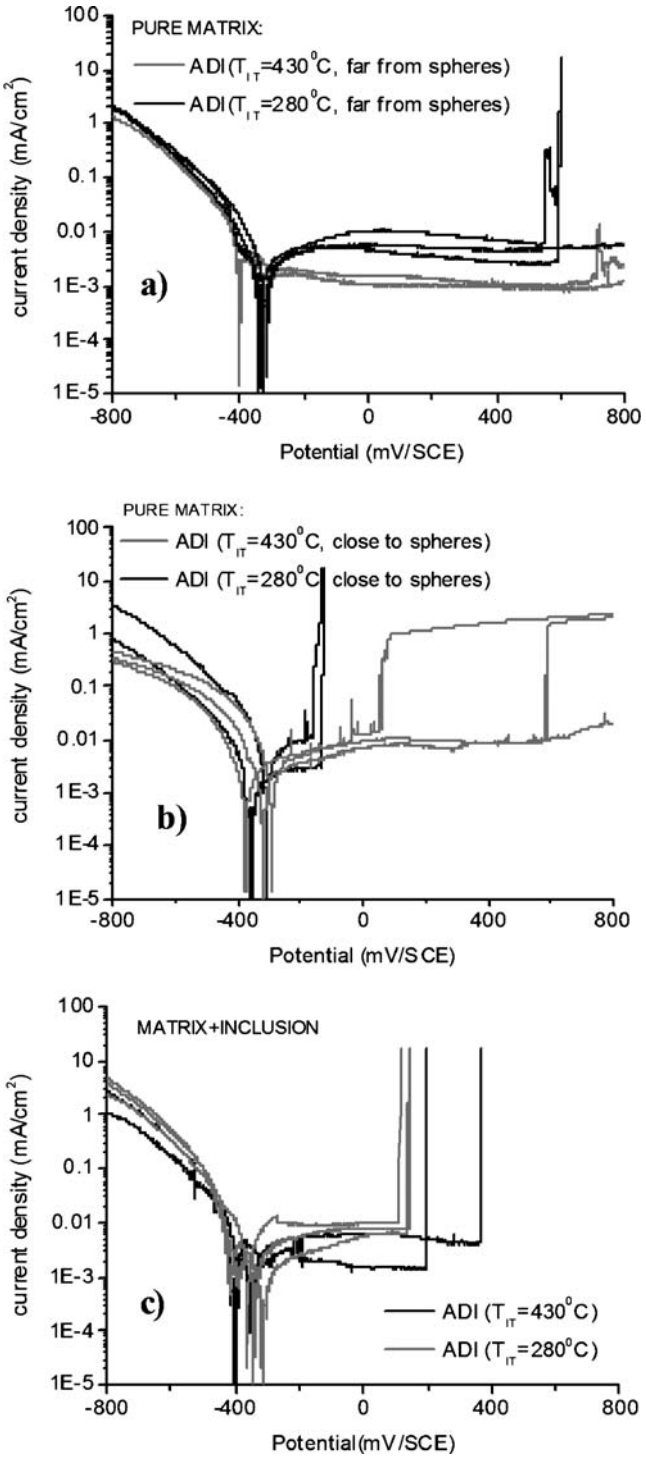

Fig. 6 Local polarisation curves at 1 mV/s determined on sites containing (**a**, **b**) the pure matrix and (**c**) the matrix with a single oxide inclusion. Experiments were performed on the types of ADI

have an irregular shape Fig. 1a,b, and matrix intrusions, matrix arches and matrix particles are visible in spheres, as it was already observed in [19]. Small ferritic particles at the graphite/matrix interface and in the graphite spheres work as local anodes, promoting corrosion processes.

Some differences between global and local polarisation curves could be observed in Figs. 4a and 6a,b. These differences could be explained by considering chronoamperometry tests performed at 675 mV/SCE and −500 mV/SCE for ADI (280 °C) ADI (430 °C), respectively. These values are located within a potential range where spheres, inclusions and the matrix located far from spheres do not dissolve (according to the local investigations described previously). Surface observations carried out after chronoamperometry revealed that corrosion only occurred in the close vicinity of some graphite spheres, as shown in Fig. 5. Therefore, the differences observed in the anodic domain between the two sets of polarisation curves (at the micro- and macroscale) were related to metallurgical effects and not induced by changes in the geometry and/or volume of the electrochemical cell used. In fact, it is difficult to identify and to do local measurements on sites such that in Fig. 5 because the density is very low at the specimen surface.

Conclusions

The influence of the austempering temperature on the microstructure and corrosion behaviour of ADI has been investigated. From global and local measurements, the following conclusions can be drawn:

- ADI austempered at 4 30°C has higher corrosion resistance than ADI austempered at 280 °C. This was related to greater coarsening of the austenite grains, broad ferrite needles and high volume fracture of ferrite (less ferrite/austenite interfaces). Silicon is an alloying element hindering the anodic dissolution of alloy.
- Corrosion of ADI specimens starts at graphite/matrix interfaces and oxide inclusions. These interfaces have an irregular shape. It was proposed that small ferritic particles at the graphite/matrix interface and in the graphite spheres work as local anodes, promoting corrosion processes. Numerical values of the current density in the passive range and pitting potentials have been provided for each sample at the microscale.

References

1. Labrecque C, Gagne M (1998) Can Metall Q 37:343, doi:10.1016/S0008-4433(98)00031-7
2. Hsu C-H, Jung-Kai R-JT (2005) Mater Sci Eng A 398:282, doi:10.1016/j.msea.2005.03.092
3. Ghaderi AR, Nili Ahmadabadi M, Ghsemi HM (2003) Wear 255:410, doi:10.1016/S0043-1648(03)00156-X
4. Prasad Rao P, Putatunda SK (2003) Mater Sci Eng A 349:136, doi:10.1016/S0921-5093(02)00633-0
5. Yang J, Putatunda SK (2005) Mater Sci Eng A 406:217, doi:10.1016/j.msea.2005.06.036
6. Janowak JF, Norton PA (1985) AFS Trans 88:123
7. Eric O, Jovanovic M, Sidanin L, Rajnovic D, Zec S (2006) Mater Des 27:617, doi:10.1016/j.matdes.2004.11.028
8. Zimba J, Simbi DJ, Navara E (2003) Cement Concr Compos 25:643, doi:10.1016/S0958-9465(02)00078-1
9. Darwish N, Elliot R (1993) Mater Sci Technol 9:882
10. Heydarzadeh Sohi M, Nili Ahmadabadi M, Bahrami Vahdat A (2004) J Mater Process Technol 153-154:203, doi:10.1016/j.jmatprotec.2004.04.308
11. Hemanth J (2000) J Mater Process Technol 101:159, doi:10.1016/S0924-0136(00)00424-6
12. Pepe A, Galliano P, Cere S, Aparicio M, Duran A (2005) Mater Lett 59:2219, doi:10.1016/j.matlet.2005.03.001
13. Krawiec H, Stypuła B, Stoch J, Mikołajczyk M (2006) Corros Sci 48:595, doi:10.1016/j.corsci.2005.02.019
14. Krawiec H, Vignal V, Banas J (2006) J Electrochem Soc 153:B231, doi:10.1149/1.2197635
15. Bohni H, Suter T, Assi F (2000) Technol Surf Coat 130:80, doi:10.1016/S0257-8972(00)00681-2
16. Putatunda SK (2001) Mater Sci Eng A 297:31
17. Roberts CS, Aime T (1953) J Met 197:203
18. Pourbaix M (1974) Atlas of electrochemical equilibria in aqueous solution, 2nd English edition, Chapter IV. National Association of Corrosion Engineers, Houston, Texas, USA, pp 452–455
19. Monchoux JP, Verdu C, Tougeres G, Reynaud A (2001) Acta Mater 49:4355, doi:10.1016/S1359-6454(01)00230-0